ADVANCED STEREO HIGH-SPEED PIV IN AN ANNULAR CASCADE WITHOUT CLEARANCE: EVIDENCES OF ROTATING INSTABILITY

J. Peter, B. Pardowitz, M. Eck, L. Enghardt, D. Peitsch, P.U. Thamsen

Technische Universität Berlin, Chair of Fluid System Dynamics, Berlin, Germany,
Julija.Peter@tu-berlin.de, Paul-Uwe.Thamsen@tu-berlin.de

German Aerospace Center (DLR), Engine Acoustics Department, Berlin, Germany,
Benjamin.Pardowitz@dlr.de, Lars.Enghardt@dlr.de

Technische Universität Berlin, Chair of Aero Engines, Berlin, Germany,
Mario.Eck@tu-berlin.de, Dieter.Peitsch@tu-berlin.de

ABSTRACT

Rotating Instability (RI) induces noise, triggers blade vibrations and is a potential indicator for critical operating conditions in axial compressors. Despite numerous studies, the source of RI is not completely understood. The objective of the present study is to give further insight into the basic mechanism of RI by means of advanced Stereo High-Speed Particle Image Velocimetry (PIV) applied to an annular compressor cascade without clearance. In particular, results of the PIV measurements visualize the predominant flow mechanism corresponding to RI. The experiments were conducted at an inflow Mach number of Ma = 0.4. Additional reference sensors captured the time-resolved pressure fluctuations synchronously to the optical measurements. By using correlation techniques between the PIV flow field and the reference sensor data, discrete vortex structures corresponding to the RI modes could be identified and localized. As a verification of the PIV results, the steady PIV flow velocity vectors are compared to results from an oil flow visualization technique. Overall, the present investigations point out that the general flow mechanism of RI is similar in compressor cascades with and without tip clearance.

KEYWORDS

ANNULAR CASCADE, COMPRESSOR, CIRCUMFERENTIAL MODES, ROTATING INSTABILITY, STEREO HIGH-SPEED PIV, UNSTEADY VORTEX STRUCTURES

NOMENCLATURE

f	frequency
i	incidence
m	mode order
Ma	Mach number
p	pressure
r	radius
Re	Reynolds number
u, v, w	velocity components in x,y,z direction
$\tilde{u}, \tilde{v}, \tilde{w}$	velocity fluctuation components in x,y,z direction

INTRODUCTION

Rotating Instability (RI) is a phenomenon observed in axial compressors at off-design conditions e.g. near stall predominantly with large clearances. RI also occurs in radial compressors and low pressure turbines (Truckenmüller (2003), Zhang et al. (2013), Raitor and Neise (2008), Cavazzini et al. (2012)). It potentially induces noise, triggers blade vibrations (Kameier and Neise (1997), Haukap (2005), Holzinger et al. (2016)) and is considered to be a potential indicator for critical operating conditions like stall and surge (Young et al. (2013)). The reliable detection of RI and better understanding about this phenomenon will provide a contribution to the development of safer, more efficient and noise reduced compressors. Therefore, fundamental studies on RI, which is typically associated with a rotor, are performed in two-dimensional or annular rows of stationary blades (Ulbricht (2002), Weidenfeller (2002), Mailach (2001)), where the swirl flow is simulated by inlet guide vanes.

Spectral characteristics, such as side-by-side peaks in the nearfield corresponding to circumferential modes with a dominant mode order below the first blade passing frequency (BPF), can be identified with single point measurements applied to the casing in rotor configurations and to the hub in the stator configurations near the leading edge (LE). Pardowitz et al. (2012a) pointed out that each RI mode in the modal pattern occurs stochastically distributed in time. The modes of different order appear independently of each other. The order of the dominant mode m with the corresponding frequency f depends on operating conditions and geometrical parameters (Pardowitz et al. (2014) and (2015a)).

Existing models assume that RI is caused by the unsteady blade tip vortex system and its interactions over passages in the circumferential direction (Mailach et al. (2001), Schrapp (2008)). However, previous work by the authors has revealed the occurrence of RI in configurations without clearance and thus without the blade tip vortex. Pardowitz et al. (2015a) observed the RI in configurations with a shrouded rotor and Beselt et al. (2013) proved RI in an annular cascade without clearance. Based on the findings of these studies, Pardowitz et al. (2012a), (2013), (2014) developed a new hypothesis about the RI source mechanism as shear layer instability due to the separation. The instability waves of different wavelengths are generated stochastically in a shear layer resulting from a back-flow extending over the whole circumference. However, this new hypothesis is not yet confirmed.

The objective of the present study is to give further insight into the basic mechanism of RI. The time-resolved 3D flow field in a single blade passage is measured by means of a Stereo High-Speed Particle Image Velocimetry (PIV) system, applied to an annular compressor cascade without clearance. The time-resolved pressure fluctuations are captured synchronously to the optical measurements. By using correlation techniques between the PIV flow field and the reference sensor data, the vortex structures corresponding to the RI modes are identified and localized. Furthermore, the steady flow field resulting from the PIV system is verified with results from an oil flow visualization technique applied at the hub in a single blade passage.

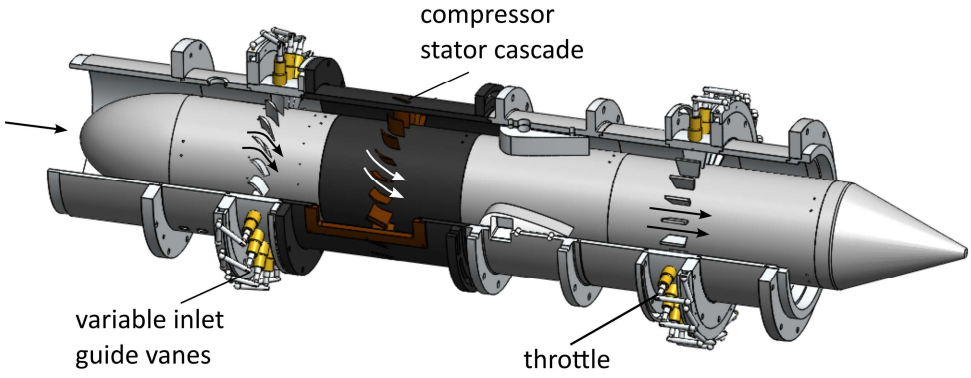

Figure 1: The test rig with the variable inlet guide vanes, the compressor stator cascade and the throttle.

EXPERIMENTAL SETUP

The experimental investigations are carried out in an annular cascade without any rotating parts, operated at TU Berlin, Chair of Aero Engines. The test rig with an overall length of l = 1.27 m consists of three blade rows with an inner radius of r_i = 86 mm and an outer radius of r_o = 120 mm: the variable inlet guide vanes (VIGV), the compressor stator cascade and the throttle (Figure 1). The investigations focus on the flow in the stator cascade. The stator row consists of 20 blades CDA (controlled diffusion airfoil) profiled, 2D-contoured and non-twisted (Ulbricht (2002)). As there are no rotating parts, the variable inlet guide vanes upstream of the stator cascade are used to form the swirl flow into the stator. The incidence angle i is adjustable in the range of i = -5° to +21°. The throttle downstream of the cascade adjusts the overall flow conditions. A more detailed description of the test rig is given in Beselt et al. (2014).

The modular experimental setup with non-rotating parts and an optical access into the stator cascade enables the application of optical measurements. In previous studies by the authors, the occurrence of the phenomenon RI was proved in the described test rig with varied aerodynamic and geometrical parameters (Beselt et al. (2013) and (2014), Pardowitz et al. (2012a) and (2013)). The typical spectral and modal pattern was identified and localized at special operating conditions. The present study focuses on investigations in a configuration with 20 blades without hub clearance with an inflow Mach number of Ma = 0.4 and an incidence angle of i = 12.8°.

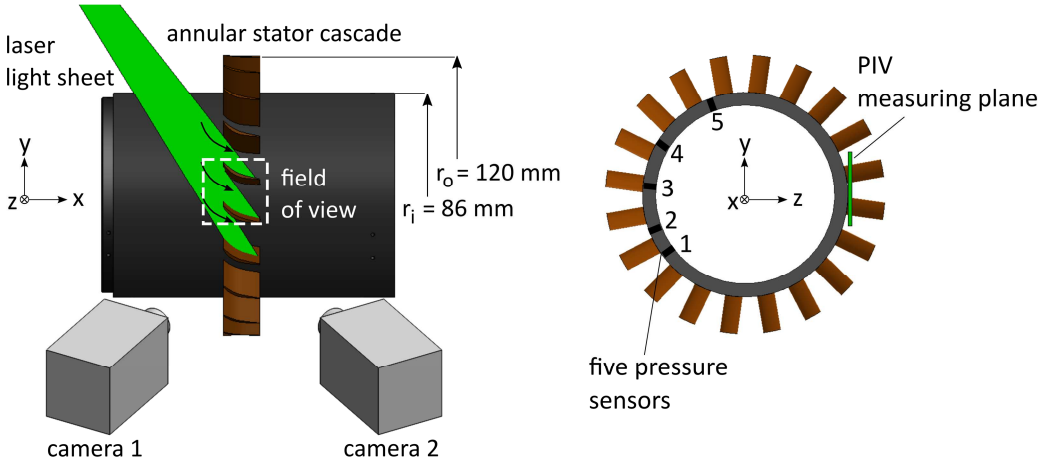

Figure 2: Application of High-Speed PIV system and pressure sensors in an annular cascade.

Velocity Field Measurement

A Stereo High-Speed PIV system is used to measure the unsteady flow field in a single blade passage (Figure 2). The DEHS (Di-Ethyl-Hexyl-Sebacat) seeding was added into the settling chamber upstream of the test rig. The Quantronix Darwin PIV-100 laser (30 mJ/pulse at f_{rep} = 1 kHz) with a wavelength of λ = 527 nm was used to illuminate the seeding particles. A repetition rate of 5 kHz with a time delay between two laser pulses of 5-6 µs was chosen to achieve a mean particle shift of about 4-5 pixels. A laser light sheet was formed by the light sheet optics. Two Photron Fastcams SA1.1 with 768x768 pixel and 10 kfps recorded the scattered light of the particles, illuminated by a formed light sheet. To achieve the Scheimpflug condition, two tilt mounts were used due to the angular displacement of the cameras in a stereoscopic application. Furthermore, the hub as well as the blades were coated with a rhodamine b-doped paint to reduce the reflections and thus to increase the quality of image. A synchronizer by ILA Intelligent Laser Applications GmbH couples the hardware components of the PIV setup. PIVview3C software was used for data acquisition and the raw image data analysis. In summary, the 3D time-resolved flow field was measured in planes tangential to the hub with an overall measuring time of approximately two seconds. Based on the Nyquist theorem the unsteady flow field is captured with a resolution of up to 2.5 kHz, suitable for the investigated flow phenomena as observed below 1 kHz. In previous

studies the occurrence of RI was observed predominantly near the hub. For this reason, the present paper focuses on the measurements in the hub region.

Pressure Measurement

The time-resolved pressure fluctuations are captured synchronously to the optical measurements by using five ¼´´ condenser microphones as reference sensors (G.R.A.S. type 40BP-S sensors). The microphones were placed circumferentially (Figure 2), mounted at the hub flush with the wall near the leading edge upstream of the stator. The data was recorded during 120 s with a sampling frequency of 102.4 kHz. Within this measurement period, the PIV system captured the time-resolved flow field.

Data Synchronization

A combined analysis of the pressure and PIV data requires the synchronization of the velocity and the pressure data. Therefore two camera signals were recorded in addition to the pressure data. The camera recording signals were used to define the start and the end of the PIV measurement. The camera exposure signal provides the times for the acquisition of velocity data. This allowed the assignment of pressure to velocity data and the down sampling of the pressure data to the PIV sampling frequency of 5 kHz.

METHODS

The detection of the modal RI events in the PIV data is difficult due to the short measurement duration. Therefore a combined analysis with the synchronized pressure data was used. The modal events were first detected in the pressure data. The resulting signals were correlated with the PIV data to determine time intervals at which the modal events occur intensely.

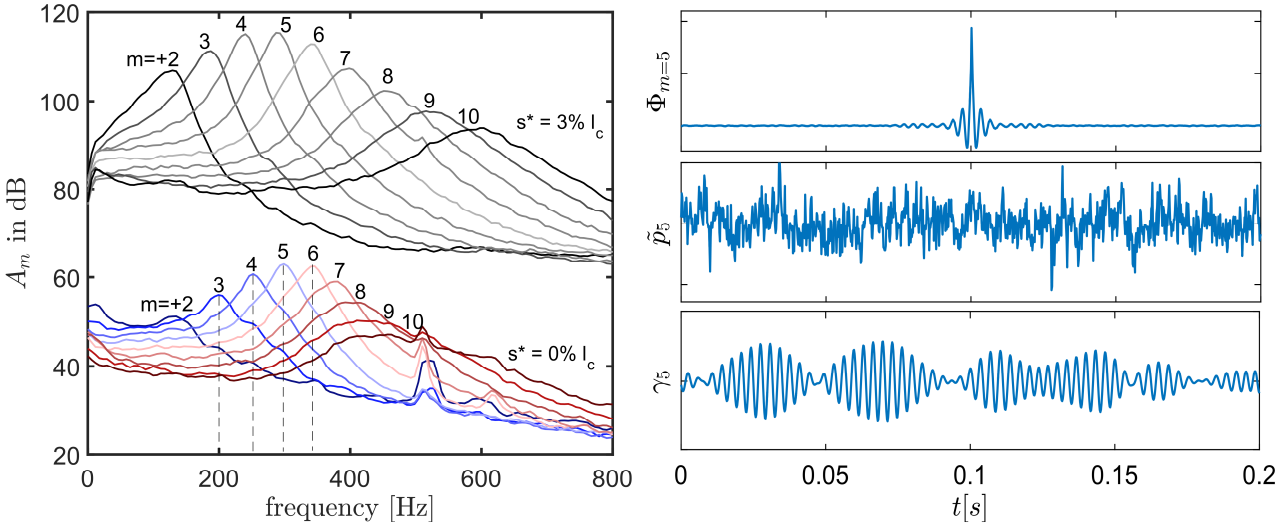

Figure 3: Left: Circumferential mode amplitudes A_m of order m = +2,…,10 measured in the annular cascade near the leading edge at Mach number of Ma = 0.4 and an incidence angle of i = 12.8° with the hub clearance (based on chord length) of s^* = 0% l_c and s^* = 3% l_c. Right: Modal event Φ_m of order m = 5, the pressure data $\tilde{p}_5$ of sensor 5 and the correlation γ_5 between the modal event and the pressure data.

Detection of Modal Events in Pressure Data

A circumferential mode decomposition of the unsteady pressure fluctuations $\tilde{p}(\varphi_j, t)$ (Pardowitz et al. (2012a) and (2013)), measured with a ring of twenty sensors in a previous study (Beselt 2016), gives an insight into the azimuthal modes (Figure 3, left). The temporal behavior of

the mode amplitudes $\tilde{A}_m$ is determined by a spatially discrete fourier transform (DFT) analysis over N_φ sensors with its position φ_j for different circumferential modes of order m (Eq. 1).

$$\tilde{A}_m(t) = \frac{1}{N_\varphi}\sum_{j=0}^{N_\varphi-1}\tilde{p}(\varphi_j, t)\cdot e^{-im\varphi_j} \tag{1}$$

The modal event Φ_m can be obtained for each mode m by means of auto-correlation (Eq. 2). Therefore the real part of the modal time signal $\Re\{\tilde{A}_m\}$ is used. The modal event $\Phi_{m=5}$ for the mode of order $m = 5$ is illustrated in Figure 3, right.

$$\Phi_m(\tau) = \lim_{T\to\infty}\frac{1}{2T}\int_{-T}^{+T}\Re\{\tilde{A}_m(t)\}\Re\{\tilde{A}_m(t+\tau)\}dt \tag{2}$$

To identify the modal events of the mode order m, the modal event Φ_m is correlated with the signal of each pressure sensor $\tilde{p}_i$ (Eq. 3). The correlation γ_5 between the pressure signal of the sensor 5 and the modal event $\Phi_{m=5}$ is displayed exemplarily in Figure 3, right.

$$\gamma_{m,i}(\tau') = \lim_{T\to\infty}\frac{1}{2T}\int_{-T}^{+T}\Phi_m(\tau+\Delta t_{m,i})\tilde{p}_i(\tau+\tau')d\tau \tag{3}$$

The microphones are unevenly distributed circumferentially around the cascade. Thus, each sensor measures the modal event of order m with a characteristic time delay. The time delay between the sensors depends on the order m and the corresponding frequency f_m, as well as the angular offset $\Delta\varphi_i$. It is calculated according to the following formula:

$$\Delta t_{m,i} = \frac{\Delta\varphi_i\cdot m}{2\pi\cdot f_m} \tag{4}$$

Afterwards, the correlation function is averaged over the two microphones with the smallest distance to the PIV evaluation window:

$$\gamma_m(\tau') = \frac{1}{2}\left(\gamma_{m,4}(\tau') + \gamma_{m,5}(\tau')\right) \tag{5}$$

Detection of Modal Events in Velocity Data

The time-resolved 3D-field is described with three velocity fluctuation components: the axial velocity $\tilde{u}$, the tangential velocity $\tilde{v}$ and the radial velocity $\tilde{w}$ in the measuring plane tangential to the hub. It should be noted that in the annular cascade the velocity component in circumferential direction and the radial component perpendicular to the circumferential velocity result from combinations of the components $\tilde{v}$ and $\tilde{w}$. To identify the modal events in these components, the cross-correlation between the components and the correlation function γ_m is determined according to the following formulas (Pardowitz et al., (2015b)):

$$\begin{aligned}
\hat{\Phi}_{\tilde{u},m}(\tau'') &= lim_{T\to\infty}\frac{1}{2T}\int_{-T}^{+T}\gamma_m(\tau')\tilde{u}(\tau'+\tau'')d\tau' \\
\hat{\Phi}_{\tilde{v},m}(\tau'') &= lim_{T\to\infty}\frac{1}{2T}\int_{-T}^{+T}\gamma_m(\tau')\tilde{v}(\tau'+\tau'')d\tau' \\
\hat{\Phi}_{\tilde{w},m}(\tau'') &= lim_{T\to\infty}\frac{1}{2T}\int_{-T}^{+T}\gamma_m(\tau')\tilde{w}(\tau'+\tau'')d\tau'
\end{aligned} \tag{6}$$

The described analysis, which can be used for each measuring plane, enables a three dimensional visualization of flow phenomena in the area captured by the PIV system.

RESULTS

In the following sections the results for an operating point with an inlet Mach number of $Ma = 0.4$, a chord based Reynolds number of $Re = 300\,000$ and an incidence angle of $i = 12.8°$ are shown. At first the steady flow field, resulting from PIV measurement and the oil visualization, is analyzed. In the following sections the results of the spectral analysis of PIV and pressure data as well as the results of the modal event detection are presented, with a focus on the dominant mode of order $m = 5$.

Steady Flow Field

Oil flow visualization

Oil flow visualization was applied in order to gain information about the general flow topology inside the compressor stator cascade without hub clearance. The oil mixture being composed of thick liquid paraffin oil with blue fluorescent pigments was painted onto the hub wall. The resulting streakline pattern is displayed in Figure 4, left. For a better overview, most of the streaklines are re-drawn with thin solid white lines, where the flow direction is indicated by small arrows. Separation lines are highlighted by thick solid white lines, whereas attachment lines are represented by thick dashed white lines. Furthermore, the pattern contains singularities like saddle points (SP) and focus points (FP).

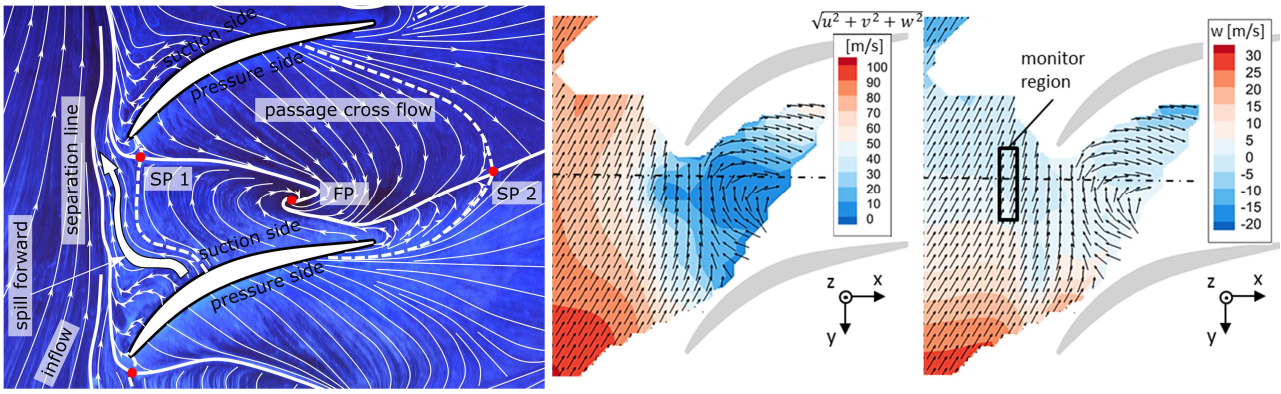

Figure 4: Steady Flow field. Left: Oil flow visualization on the hub of the annular cascade. Middle: Time averaged flow field in the plane with the radius of $r = 86.5$ mm, tangential vectors in the *xy*-plane and the velocity magnitude as contour are illustrated. Right: Time averaged flow field in the plane with the radius of $r = 86.5$ mm, tangential vectors in the *xy*-plane and the radial (out of plane) velocity component *w* as contour are illustrated.

The oil flow picture shows that the entire incoming boundary layer detaches along a separation line upstream of the cascade entry. This special streakline pattern with a continuous separation line is well known from previous investigations in a compressor stator with hub clearance. At an operating point, where RI is present, it was found that the leakage flow spilling around the leading edge of the neighboring blade caused blockage and forced the inflow boundary layer to separate from the hub over the entire circumference of the cascade. In the present configuration without tip clearance, the blockage is caused by a combination of several secondary flow phenomena being extended and intensified at an incidence angle of $i = 12.8°$. The flow inside the passage is dominated by a corner separation and the passage cross flow. The corner separation is responsible for the formation of a spiral node (FP) on the hub wall, at which a large amount of passage cross flow lifts off the surface. Furthermore, the roll-up point of the horse shoe vortex is indicated by a saddle point (SP1) near the leading edge. While the pressure side leg is deflected by the cross-passage pressure gradient, the suction side leg bursts immediately downstream of its roll-up point. The vortex breakdown results in a cross-sectional expansion of the vortex core which itself interacts with the three-dimensional separation. This interaction leads to a reversed flow at the leading edge

plane. Summarizing, the low kinetic energy fluid from vortex breakdown of the horse shoe vortex and three-dimensional separation is affected by forward spilling.

PIV data

Approximately 9700 instantaneous velocity fields were captured in planes tangential to the hub during two seconds with a time delay of 0.2 ms between two fields. For each plane a time averaged flow field was created. Afterwards the planes in the hub region with r = 86.5 – 95 mm were composed to a 3D steady flow field. An averaged flow field of a single plane next to the hub with a radius of r = 86.5 mm is presented in Figure 4. In the middle, the tangential vectors in the *xy*-plane and the velocity magnitude as contour are illustrated. On the right, tangential vectors in the *xy*-plane and the radial velocity component w as contour are shown. The dashed line indicates the tangent of the measuring plane and thus the smallest distance to the hub. Additionally, the monitor region, which was used for the spectral analysis and the event detection, is depicted. To illustrate the composed 3D steady flow field, slices in *yz*-plane and *xz*-plane with tangential vectors and the contoured axial velocity component u are used (Figure 5).

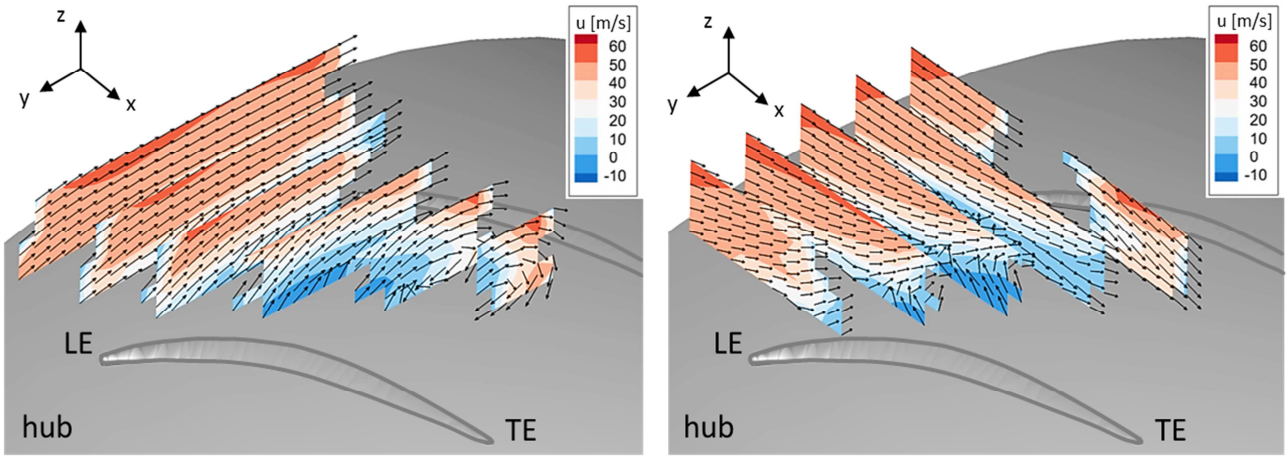

Figure 5: Composed 3D steady flow field. Left: Slices in the *yz*-plane. Right: Slices in *xz*-plane, illustrated with the axial velocity component *u* as contour and tangential vectors (LE: leading edge, TE: trailing edge).

A homogeneous inflow with a constant incidence angle is achieved by the variable inlet guide vanes. The radial distance to the hub is not equal for each y position due to the position of the light sheet. Thus, the velocity magnitude in regions with higher radial positions e.g. on the lower left is larger than the velocity magnitude in regions with smaller distance to the hub (Figure 4, middle). A region of reduced flow velocities is formed in the blade passage. The flow is decelerated and spills forward into the adjacent passage. This might be a result of secondary flow effects e.g. flow separation on the hub. Furthermore, there are regions with positive and negative values of the radial velocity component w. This indicates a flow into and out of the measuring plane due to the circumferential flow component. The strong influence of the corner separation and the passage cross flow on the flow inside the passage, revealed in the oil flow visualization, is also shown in the results of the PIV measurements. The passage vortex is displayed in the *yz*-slices of the composed 3D field (Figure 5, left). Close to the hub wall the flow moves towards the suction side of the adjacent blade and rolls up into a vortex, located in the lower third of the blade height. The upstream effect of the corner separation might be seen in the *xz*-slices of the composed 3D field (Figure 5, right). Due to the separation, the flow close to the hub, in the region near the suction side of the stator blade, is deflected towards the leading edge and to higher radii. This effect is also observed in the lower third of the blade height. Overall, the results of the PIV measurements are in good agreement with the findings of the oil flow visualization.

Spectral Analysis

To prove the existence of RI, spectral analysis (Bendat and Piersol (2011)) of the PIV data and the synchronized pressure data was performed. The power spectral density *PSD* for the pressure data of the sensor 5 and the coherence spectrum γ^2 as well as the phase spectrum φ between sensors 5 and 4 are shown in Figure 6, left. These sensors were chosen as they had the smallest distance to the PIV evaluation window (Figure 2). For the analysis, original data with the sampling frequency of 102.4 kHz and down sampled data to a sampling frequency of 5 kHz with a length of approximately of 2 s, corresponding to the PIV measurement, were used. Additionally, the averaged spectra of the reference data, measured with a ring of twenty sensors during the overall measurement time of 2 min, is depicted in Figure 6, left. The dashed lines indicate the mode frequencies for modes of order m = 3,4,5,6 (Figure 3, left). In a range of f = 150 - 500 Hz peaks in the power spectral density and in the coherence spectrum are observed. The strong pronounced peak at the frequency of 500 Hz is connected with resonance caused by the overall axial extension of the test rig (Pardowitz et al. (2012b)). However, in comparison to the reference data, the peaks in the data measured synchronously with the PIV are less pronounced. This might be due to the short evaluation time of approximately 2 s. As the modes related to RI appear stochastically and independently of each other, in the short time of 2 s few modes may appear more frequently than others. Furthermore, the seeding particles (DEHS), which are added to the flow for the PIV measurements, may disturb the synchronously captured signals by the microphones. The linear shift in the phase spectrum is caused by the propagation of RI in the circumferential direction.

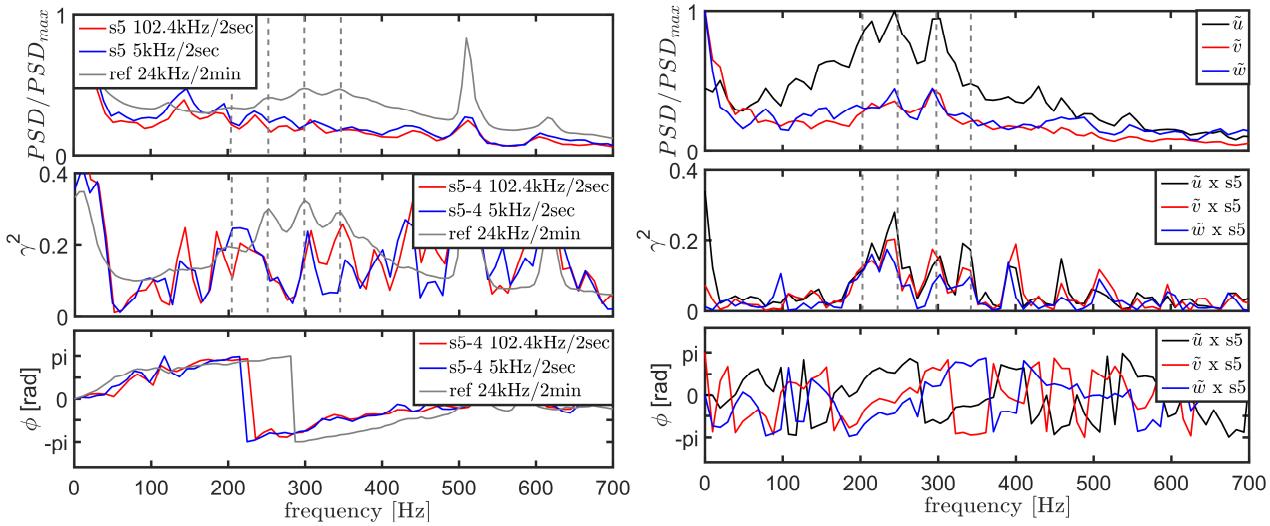

Figure 6: Spectral analysis of pressure data and the PIV data for an inflow Mach number of *Ma* = 0.4 and an incidence angle of *i* = 12.8°. Left: Power spectral densities *PSD/PSD*$_{max}$, the coherence γ^2 and the phase spectra φ of sensor 5. Right: Power spectral densities of the three velocity components and the coherence as well the phase spectra, resulting from a combined analysis of pressure and velocity data.

In studies by Beselt et al. (2013) the occurrence of RI in the annular cascade without hub clearance was proved. The results showed an influence of the clearance size on the order of the dominant mode and the intensity of RI. Obviously, the RI phenomenon occurs in the configuration used in the present study (Ma = 0.4, i = 12.8°, hub clearance of 0% l_c based on chord length) with lower intensity compared to the set-up with the hub clearance of 3% l_c (Pardowitz et al. (2015)), where much stronger side-by-side peaks were identified by identical analysis tool. The circumferential mode amplitudes for modes of order m = 2,..,10 of both configurations are depicted in Figure 3, left.

The power spectral densities for the axial, tangential and radial velocity fluctuation components $\tilde{u}$, $\tilde{v}$ and $\tilde{w}$ in the measuring plane with a radius of r = 87 mm are displayed in Figure 6, on the top right. Therefore the monitor region with an axial distance of approximately 10 mm to the leading edge, depicted in Figure 4, was used. The RI signature is present in the frequency range of f = 150 - 350 Hz, predominantly in the axial component $\tilde{u}$. This has already been shown in earlier studies (Pardowitz et al. (2013) and (2015b)). The highest amplitudes are observed for the frequencies corresponding to the modes of order mode m = 3, 4, 5. However, the highest amplitudes of the circumferential modes measured with a ring of twenty sensors (Figure 3, left) were identified for modes of order m = 4, 5, 6 with the dominant mode of order m = 5. This might be due to the short measurement time of the PIV measurement of approx. 2 s. Additionally, the spatial extension of the RI signature for the mode order m = 5, corresponding to a frequency of approximately 300 Hz, is displayed for the plane with r = 87 mm in Figure 7. The highest amplitudes are observed upstream of the stator blades, with an axial distance of approximately 10 mm to the leading edge. This region corresponds to the separation line, identified in the oil flow visualization. Another region with high amplitudes is found to be in the passage near the suction side of the stator blade with an axial distance of up to 5 mm to the leading edge. The coherence spectrum between the pressure data and the velocity components is displayed in Figure 6, on the middle right. Peaks between 200 Hz and 500 Hz with a difference of approximately 50 Hz between each other are observed in the combinations with all three velocity components. The peaks in the power spectral densities of the PIV data and the coherence spectrum between the PIV and the pressure data match the peaks of the reference spectra for the modes of order m = 3, 4, 5, 6 well. The shift in peaks might appear due to the frequency resolution of approx. 5 Hz for the reference data and 10 Hz for the synchronously captured data. The step shaped shift in the phase spectrum in the range between 150 Hz and 400 Hz in Figure 6, on the bottom right appears due to circumferential movement.

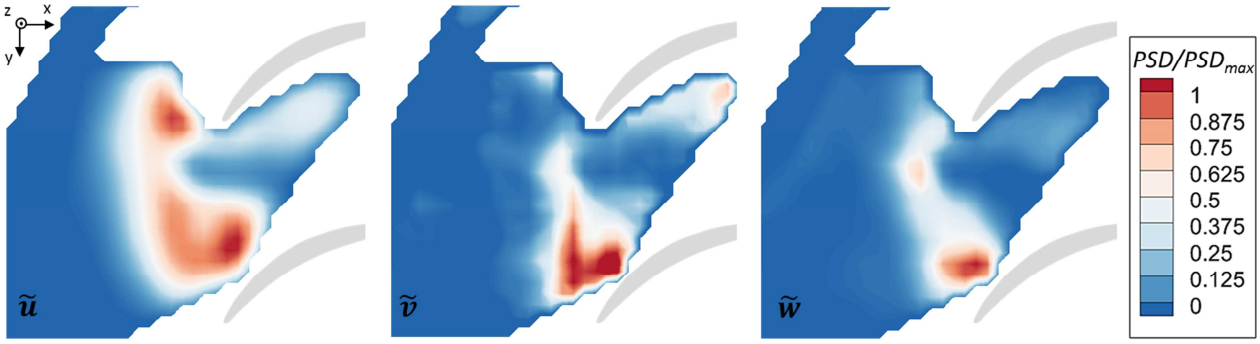

Figure 7: Power spectral densities for the RI mode of order m = 5, corresponding to a frequency of 300 Hz, for the three velocity components in the measuring plane with r = 87 mm, for an inflow Mach number of Ma = 0.4 and an incidence angle of i = 12.8°.

Modal Event of order m = 5

The modal event for the dominant mode of order m = 5 is determined according to Eq. 6 by means of cross-correlation in the measuring plane with the radius of r = 87 mm, as shown in Figure 8. The tangential vectors and the axial velocity fluctuation components $\tilde{u}$ are used as contours for the illustration. For the mode order m = 5 one vortex structure covers several blade passages. Consequently, it is not possible to illustrate a structure in the whole within one time step. The structures move in the circumferential direction. In Figure 8, a change in the direction of the flow is apparent. The flow moves out of ($\tau'' = 1.0$ ms) and into the passage ($\tau'' = 2.6$ ms). In between, vortex cores are identified, e.g at $\tau'' = 1.6$ ms. Thereby, the rotational direction of following structures alternates from counterclockwise to clockwise. The sequence repeats several times until the structures disintegrate again. A characteristic period of one sequence takes approximately T = 3.2 - 3.4 ms. This matches the corresponding frequency f = 300 Hz = $1/T$ of the

mode m = 5. The modal structures over the whole circumference of the annular cascade are illustrated in Figure 9. Therefore, the PIV results in the measuring plane with r = 87 mm were extended in the circumferential direction. The region, which was used for extension, is depicted in Figure 9, left. The modal structures are clearly visible. The circumferential extension of the structures matches the wavelength corresponding to the mode of order m = 5. It should be noted that the distribution is not perfectly smooth. This is caused by the limited repetition rate of the PIV system and the tangential position of the measuring plane to the hub. Overall, the findings are in accordance to earlier studies by the authors (Pardowitz et al. (2014), (2015b)).

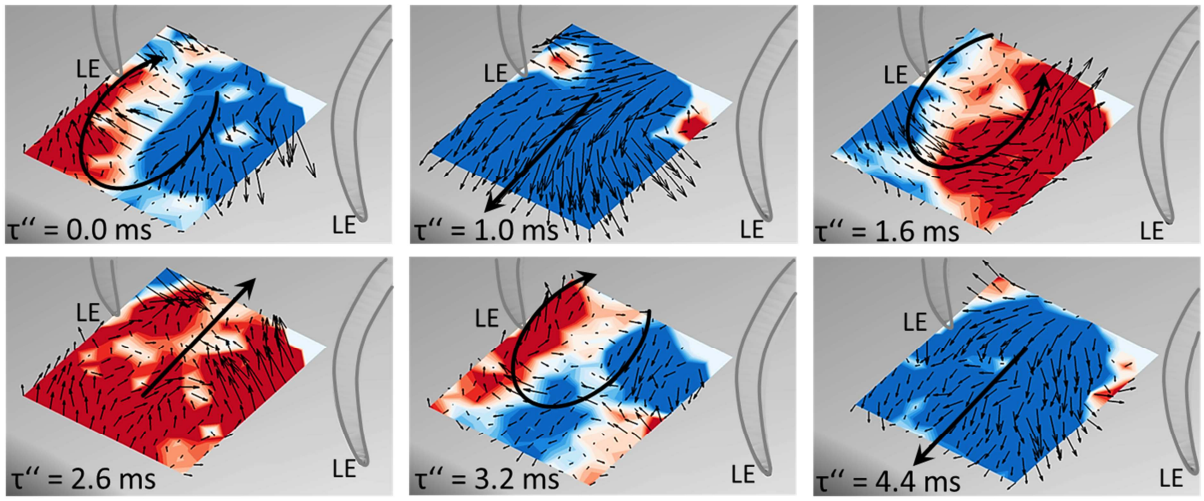

Figure 8: Modal event for the mode order m = 5 at a measuring plane with radius of r = 87 mm, colored with the axial fluctuation component.

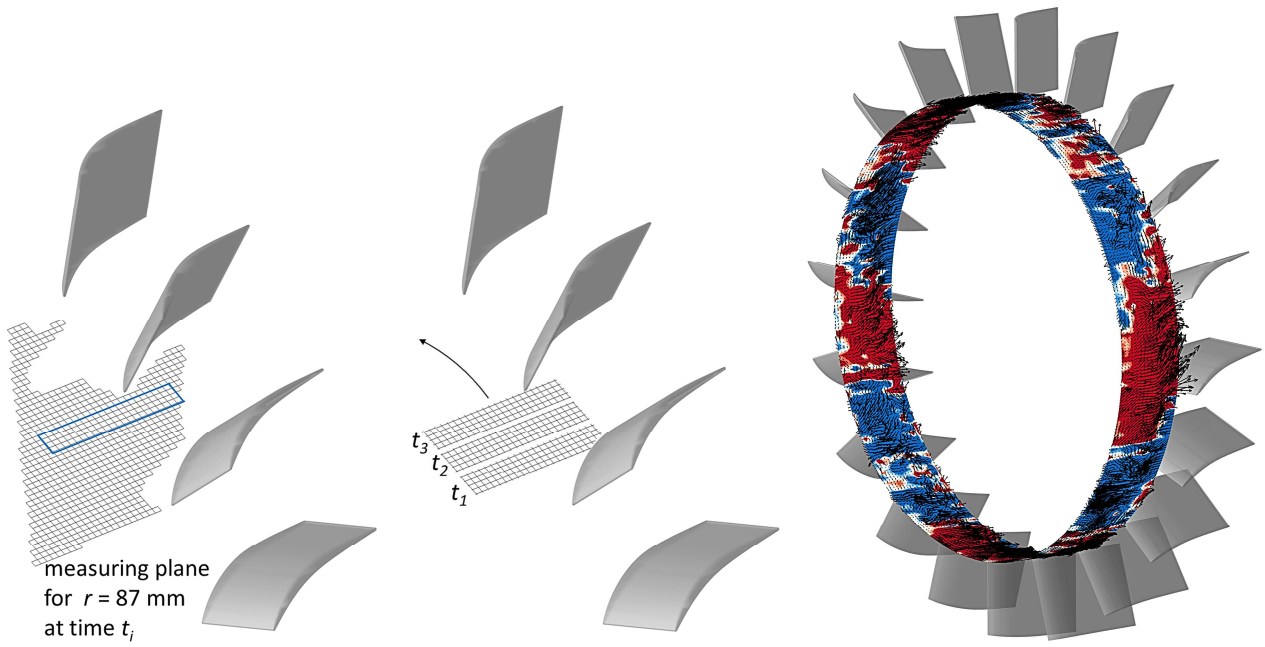

Figure 9: Left: The PIV grid of the measuring plane with radius of r = 87 mm and the selected region, used for the circumferential extension. Right: Circumferential structures corresponding to the modal event of order m = 5, colored with the axial fluctuation component.

CONCLUSIONS

The presented study was performed in an annular cascade without hub clearance at operating conditions where RI occurs. The objective was to identify and to visualize characteristic flow topology corresponding to RI in a configuration without hub clearance. The three dimensional flow field, captured by the Stereo High-Speed PIV system, showed a strong influence of the three dimensional separation and the passage cross flow on the flow inside the passage. This matches the findings of the oil flow visualization on the hub, where a separation line upstream of the leading edge over the whole circumference was observed. The separation line indicates the reversed flow over the whole circumference, which is caused by the interaction between the horse shoe vortex and the three dimensional separation. In conclusion, the breakdown of the horse shoe vortex seems to have a strong influence on the emergence of RI. In addition, it was found that the modal arrangement of radial vortex structures travelling along the continuous separation line is similar in compressor cascades with and without tip clearance. While propagating around the circumference of the compressor cascade, the radial vortices induce an alternating in- and outflow at the leading edge plane.

ACKNOWLEDGEMENTS

The work was supported by the German Research Foundation (DFG, project: Flow induced noise in turbomachinery - The rotating instability). The funding is gratefully acknowledged. The helpful discussions with our partners in the joint project and the support by Maximilian Reinhardt and Christian Donat regarding the PIV evaluation are gratefully appreciated.

REFERENCES

Bendat J.S., Piersol A.G., (2011) *Random data: analysis and measurement procedures*. John Wiley & Sons

Beselt C., Pardowitz B., v. Rennings R., Sorge R., Peitsch D., Enghardt L., Thiele F., Ehrenfried K., Thamsen P.U., (2013) *Influence of the clearance size on rotating instability in an axial compressor stator*. Proceedings of 10th European Turbomachinery Conference, Finland

Beselt C., Eck M., Peitsch D., (2014) *Three-dimensional flow field in highly loaded compressor cascade.* Journal of Turbomachinery, 136(10), 101007

Beselt Ch., (2016) *Experimentelle Untersuchung von Sekundärströmungsphänomenen in einer Verdichter-Stator-Kaskade.* PhD Thesis. TU Berlin

Cavazzini G., Dazin A., Pavesi G., Dupont P., Bois G., (2012) *Post-processing methods of PIV instantaneous flow fields for unsteady flows in turbomachines*. The Particle Image Velocimetry - Characteristics, Limits and Possible Applications, edited by P. G. Cavazzini, InTech, pp. 97–120

Haukap C., (2005) *Zur Korrelation von Schaufelschwingungen und rotierenden Strömungsphänomenen in Axialverdichtern.* PhD Thesis, TU Munich

Holzinger F., Wartzek F., Jüngst M., Schiffer H. P., Leichtfuß S., (2016) *Self-Excited Blade Vibration Experimentally Investigated in Transonic Compressors: Rotating Instabilities and Flutter.* Journal of Turbomachinery, 138(4), 041006

Kameier F., (1993) *Experimentelle Untersuchung zur Entstehung und Minderung des Blattspitzen-Wirbellärms axialer Strömungsmaschine*. PhD Thesis, TU Berlin

Kameier F., Neise W., (1997) *Rotating Blade Flow Instability as a Source of Noise in Axial Turbomachines*. Journal of Sound Vibration, Vol. 203, pp. 833–853

Mailach R., Lehmann I., Vogeler K., (2001) *Rotating Instabilities in an Axial Compressor Originating From the Fluctuating Blade Tip Vortex.* Journal of Turbomachinery, Vol. 123, pp. 453–463

Mailach R., (2001) *Experimentelle Untersuchung von Strömungsinstabilitäten im Betriebsbereich zwischen Auslegungspunkt und Stabilitätsgrenze eines vierstufigen Niedergeschwindigkeits-Axialverdichters.* PhD Thesis, TU Dresden

Pardowitz B., Tapken U., Enghardt L., (2012a) *Time-resolved Rotating Instability Waves in an annular Cascade.* 18th AIAA/CEAS Aeroacoustics Conference, 4.-6. Juni, USA, No. 2012-2132

Pardowitz B., Tapken U., Enghardt L., (2012b) *Acoustic Resonances and Aerodynamic Interactions in an Axial Compressor Stator Stage Test Rig.* 10th Int. Conference of Flow-Induced Vibration (& Flow Induced Noice), Dublin, Ireland

Pardowitz B., Tapken U., Sorge R., Thamsen P.-U., Enghardt L., (2013) *Rotating Instability in an Annular Cascade: Detailed Analysis of the Instationary Flow Phenomena.* ASME J Turbomach, Vol. 136, No. 6

Pardowitz B., Tapken U., Neuhaus L., Enghardt L., (2014) *Experiments on an axial fan stage: Time resolved analysis of Rotating Instability modes.* J. Eng. Gas Turbines Power, Vol. 137, No. 6

Pardowitz, B., Moreau A., Tapken U., Enghardt L., (2015a) *Experimental identification of rotating instability on an axial fan with shrouded rotor*. Proceedings of the Institution of Mechanical Engineers, Part A: Journal of Power and Energy, 229(5):520–528

Pardowitz B., Peter J., Tapken U., Thamsen P.U., Enghardt L., (2015b) *Visualization of Secondary Flow Structures Caused by Rotating Instability: Synchronized Stereo High-Speed PIV and Unsteady Pressure Measurements.* Proceedings of 45th AIAA Fluid Dynamics Conference, USA

Raitor T., Neise W., (2008) *Sound generation in centrifugal compressors*. Journal of Sound and Vibration, Vol. 314, No. 35, pp. 738 – 756

Schrapp H., (2008) *Experimentelle Untersuchungen zum Aufplatzen des Spaltwirbels in Axialverdichtern.* PhD Thesis, TU Braunschweig

Truckenmüller F., (2003) *Untersuchungen zur aerodynamisch induzierten Schwingungs-anregung von Niederdruck-Laufschaufeln bei extremer Teillast.* Ph.D. Thesis, Universität Stuttgart

Ulbricht I., (2002) *Stabilität des stehenden Ringgitters.* PhD Thesis. TU Berlin

Weidenfeller J., (2002) *Experimentelle Untersuchungen der stationären und instationären Strömung eines Axialverdichtergitters.* PhD Thesis. University Kassel

Young A., Day I., Pullan G. (2013) *Stall warning by blade pressure signature analysis.* Journal of Turbomachinery, 135(1), 011033

Zhang L. Y., He L., Stuer H., (2013) *A Numerical Investigation of Rotating Instability in Steam Turbine Last Stage*. Journal of Turbomachinery, Vol. 135, pp. 011009 1–9